THE JOURNAL OF PHYSICAL CHEMISTRY C

Article

Cite This: J. Phys. Chem. C 2019, 123, 16359−16365

pubs.acs.org/JPCC

Theoretical and Experimental Investigation of 2D Hematite

A. C. M. Padilha,*[,†] M. Soares,[‡] E. R. Leite,[†,‡] and A. Fazzio[†,§]

[†]Brazilian Nanotechnology National Laboratory (LNNano)/CNPEM, Campinas 13083-970, Brazil

[‡]Department of Chemistry, Federal University of São Carlos, São Carlos 13565-905, Brazil

[§]Center for Natural and Human Sciences, Federal University of ABC, Santo André 09210-580, Brazil

Supporting Information

ABSTRACT: Novel two-dimensional non-van der Waals materials have been reported, boosting efforts to probe their properties and identify key applications. In this work, we report the synthesis, by means of a novel route via sonication of synthetic hematite, and characterization by transmission electron and atomic force microscopy of samples composed of two-dimensional hematite ([001]-cut layered α-Fe_2O_3). Microscopy images show a layered material with a handful of possible crystalline orientations, of which the [001] is the most abundant, presenting thickness of up to approximately 100 nm. Next, we employed first-principles calculations to study their structural stability and evaluate their thickness distribution. The stability of single, double, and triple layered structures is confirmed by phonon spectra and the formation energy is obtained, pointing out to the possibility of few layers, freestanding, stable samples. Further statistical modeling suggests that even though such thin samples are stable, their abundance is very small in comparison to thicker layers. We show that the antiferromagnetic ordering of the bulk phase is preserved in the nanostructured material, from the double-layered sample onward; however, a nonzero magnetization arises due to distinct localized moments in surface Fe atoms. Finally, our calculated band structures present narrower gaps in the layered structures in comparison to the bulk, and a charge-trapping acceptor level is identified at the surface Fe atoms.

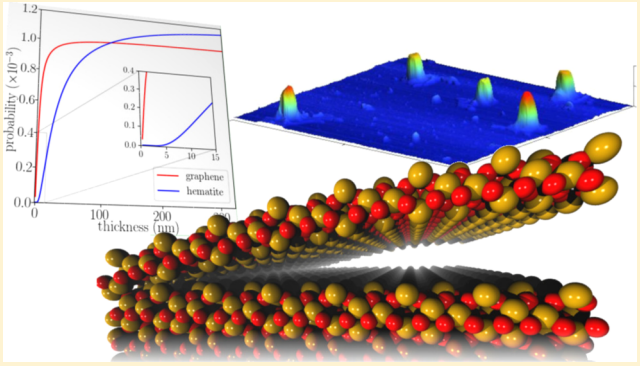

INTRODUCTION

Since the discovery of graphene, the prototypical two-dimensional (2D) material,[1] great efforts have been employed into the investigation of this class of low-dimensional materials. Their applications in photocatalysis, spintronic devices, and topological insulators[2−10] have made 2D materials one of the most active areas of research in condensed matter physics and materials science in the last decade.

The majority of reported 2D materials can be described as stacked van der Waals layered structures.[11,12] However, recent reports point to the existence of stable non-van der Waals 2D materials, synthesized via liquid exfoliation of oxide ores.[13−15] Among these, the [001]-cut layered α-Fe_2O_3 (2D hematite) has been predicted as a suitable material for photocatalytic applications, and distinct magnetic and electronic properties with respect to the bulk material have been reported.[13] Their electronic structure, magnetic properties, and structural stability from the point of view of theoretical first-principles calculations still need to be elucidated. Further experimental data reporting on the structural motifs and crystalline orientations of exfoliated samples is also needed to establish a protocol capable of obtaining these materials on a large scale.

In this work, we report the synthesis, via a wet chemical route and subsequent exfoliation using sonication, and characterization by means of high-resolution transmission electron microscopy (HRTEM) and selected area electron diffraction (SAED) of 2D hematite. Here, we used a synthetic hematite instead of an oxide ore. Characterization of the morphology of the sample was done via atomic force microscopy (AFM). To further investigate the properties of this novel material, we study the electronic, structural, and magnetic properties of 2D hematite using computational simulations based on density functional theory (DFT). We compare the electronic structure, phonons spectra, and magnetic orderings of bulk hematite with the single-layered (1L, Figure 1), double-layered (2L), and triple-layered (3L) structures obtained by cutting the original structure along the [001] planes. First, we report the experimental procedure to obtain the samples and to further characterize them. Next, we explain the computational methods employed in this work. Experimental results are reported in sequence, and we summarize the computational and theoretical results obtained for the structural, electronic, and magnetic properties. A discussion of the obtained results, emphasizing the structural stability, the distinct band gaps, and the microscopy data obtained for the exfoliated structures, is presented briefly prior to our conclusions.

Received: February 1, 2019
Revised: June 10, 2019
Published: June 12, 2019

DOI: 10.1021/acs.jpcc.9b01046
J. Phys. Chem. C 2019, 123, 16359−16365

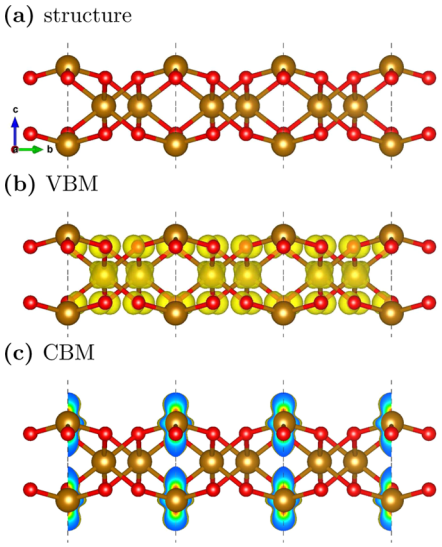

Figure 1. (a) Crystalline structure of 1L α-Fe_2O_3 and the corresponding real-space projections (constant density of 0.01 e Å^{-3}) of the valence band maximum (VBM) (b) and conduction band minimum (CBM) (c). Fe atoms are golden large spheres, while O atoms are red smaller spheres.

EXPERIMENTAL SETUP

Sample Preparation. Layered hematite was obtained from hematite nanospheres sintered in a conventional furnace. The synthesis was performed following a procedure by Gou et al.,[16] where 1 mmol iron(III) nitrate nonahydrate, 2 mmol sodium citrate, and 2.5 mmol urea (Sigma-Aldrich) were dissolved in 30 mL of deionized water. Subsequently, the solution was submitted to the hydrothermal process at 160 °C for 8 h, and the pressure at equilibrium was 1.2×10^6 Pa. A brown-yellow material was obtained, and it was collected by centrifugation (11 000 rpm for 15 min) and washed several times with deionized water. Finally, the resulting powder was dried in air at 60 °C overnight. In Figure S4a (see Supporting Information), we present an image acquired using a field emission scanning electron microscope (FE-SEM) where we observe nanoparticles with spherical morphology and average particle size of 196 nm.

The obtained nanospheres (see Figure S4a) were compacted at 750 kgf cm^{-2} into a pellet 6 mm in diameter. In the sequence, using a conventional furnace, the pellet was sintered at 500 °C for 2 h and at 900 °C for 5 h. In Figure S4b, we present a fractured image of a sintered pellet, where we observed a flat structure with a plate-type morphology, an indication of a 2D structure. To further investigate the morphology, we performed the procedure reported by Puthirath Balan et al.,[13] which consists of pulverizing the sintered pellet into a fine powder using mortar and pestle with acetone as a wetting medium. Next, 5 mg of the obtained powder was dispersed into 20 mL of *N*,*N*-dimethylformamide (DMF, Sigma-Aldrich) and sonicated in a bath sonicator for 50 h. The maximum temperature reached in this experiment was 60 °C. Finally, a suspension was obtained as presented in the inset of Figure S4b.

Microscopy Setup. High-resolution transmission electron microscopy (HRTEM) and electron diffraction (ED) analysis were performed on a 200 kV JEOL JEM 2100F microscope. The exfoliated material was deposited on an ultrafine carbon grid. The ED experiments were carried out using a charge-coupled device (CCD) detector operated at 200 keV (λ = 0.025079 Å), with camera length of 20 cm and exposure time per frame around of 0.3 s. A field-emission scanning electron microscope (FE-SEM) was used for microstructural characterization of the hematite nanoparticles as well as for the characterization of the sintered hematite pellet. Atomic force microscopy (AFM) images were obtained using a Bruker MultiMode VIII microscope. A Si tip with a force constant of 0.4 N m^{-1} and a resonance frequency of 70 kHz were used in tapping peak force method. The samples were diluted in deionized water, and a single drop was dried on a clean Si surface at 200 °C for 2 h in a nitrogen flux. The resolution of the obtained images was 512 × 512 pixels.

THEORETICAL METHODS

The electronic structure as well as minimum-energy structures (forces < 2.5×10^{-6} eV Å^{-1}) of the hexagonal bulk, 1L as well as 2L and 3L layered hematite were obtained from ab initio methods implemented via the VASP package,[17,18] and the Perdew−Burke−Ernzerhof exchange−correlation functional[19] was used. Energy convergence (1 meV per formula unit) on *k*-points was achieved using Γ-centered meshes of 4 × 4 × 2 and 8 × 8 × 1 meshes for the bulk and layered structures, respectively. Energy cutoff was 500 eV for all calculations, and the $3d^7 4s^1$ and $2s^2 2p^4$ electrons were considered as in the valence levels of Fe and O, respectively, within the projector augmented method.[20] An effective Hubbard onsite parameter of 4 eV (U) for the Fe(d) electrons was used in all calculations,[21] following other theoretical works on the [001] surface of α-Fe_2O_3.[22−24] All images depicting structural data were generated using VESTA.[25]

Structural models for the slabs were based on the Fe-terminated surfaces (one third of the Fe sites on the surface occupied) obtained from the bulk structure.[26] These were shown to be stable in a wide range of the O chemical potential via similar theoretical methods by Rohrbach et al.[22] All atomic positions were allowed to relax, while a vacuum layer of 15 Å was kept fixed in all slab calculations. To assess the structural stability of the layered materials, i.e. to determine if these low-dimensional materials are stable in face of lattice vibration, and comparison with the bulk, phonon spectra were obtained using Phonopy.[27] For the bulk and 1L, 2L, and 3L layered structures, we used, respectively, 3 × 3 × 3 and 3 × 3 × 1 supercells built from the previously relaxed structures. The lattice constant for the layered hematite was obtained from the fitting of the Vinet et al. equation of state[28] for the 1L phase. An expression for the formation energy (ΔE_f) vs number of layers (n) was obtained by a nonlinear fitting of the form

$$\Delta E_f = E_0 + E_1 n^{\lambda} \quad (1)$$

where E_0, E_1, and λ are the parameters of the fitting. The physical meaning of the parameters E_0 and E_1 are the bulk formation energy, i.e., the energy in the limit $n \to \infty$ (this statement is due to the fact that λ obtained from the fitting is negative, see discussion further), and the marginal energy gain or loss per additional layer, respectively. We relaxed the structures composed from a single layer up to seven layers for the fitting, keeping the fixed lattice constant at its experimental bulk value. The reference phases for the calculation of ΔE_f were the molecular O_2 and the metallic bulk Fe^{FCC} whose structural parameters were relaxed and the total energies were converged to less than 1 meV per atom. Except when explicitly stated, in all calculations, the most stable magnetic ordering AF_1 was considered (antiferromagnetic coupling between Fe layers along the z-direction, more details further). Using the formation

DOI: 10.1021/acs.jpcc.9b01046
J. Phys. Chem. C 2019, 123, 16359−16365

energy expression (eq 1), a simple probabilistic model is proposed to estimate the probability of obtaining a layered structure with that corresponding thickness by means of Boltzmann probability factors

$$p(n) = \frac{e^{-\beta E_1 n^{\lambda}}}{\sum_{m=1}^{\infty} e^{-\beta E_1 m^{\lambda}}} \quad (2)$$

where E_1, n, and λ are the same quantities used in eq 1 and β is 25 meV^{-1}, corresponding to room temperature.

Owing to the variety of possible magnetic orderings in hematite, we employed the spin-polarized calculations to determine the ground state of both the bulk and layered structures. For several spin configurations (σ), we obtained the total energy using a strict convergence criteria (1×10^{-8} eV) and mapped the differences of these quantities into a Heisenberg Hamiltonian[29,30]

$$H^{\sigma} = -\sum_{\langle i,j \rangle} J_{ij} \vec{S}_i \cdot \vec{S}_j \quad (3)$$

where the summation extends to the neighboring pairs of localized spins in sites i and j, J_{ij} is the exchange coupling between these sites, and $\vec{S}_i$ is a localized classical spin. Once the most stable magnetic ordering for each structure was determined, they were used for the calculation of the structural (ΔE_f and phonon spectra) and electronic (band structure and real-space projections of the electronic levels) properties.

RESULTS

Experimental Results. We characterized the material originated from the exfoliation process by high-resolution transmission electron microscopy (HRTEM) and select area electron diffraction (SAED), and the results are shown in Figure 2. The low-magnification HRTEM image shown in Figure 2a illustrates a multilayer 2D particle. At the edges of the particle, we can see different layers that characterize a 2D structure. Several other particles also exhibited the same characteristics, such as the presence of wrinkled regions (see Figure S5 in the Supporting Information), typical of materials formed by a few atomic layers.

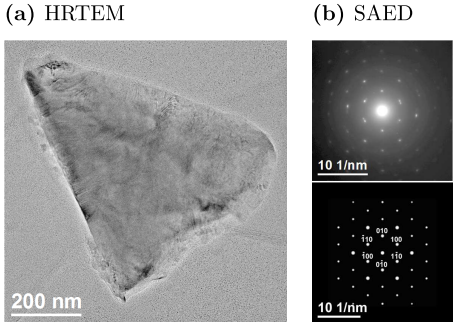

Figure 2. (a) HRTEM image of a hematite flake: (b) top: electron diffraction of a hematite flake, depicting the hexagonal motif of a [001]-cut hexagonal structure; bottom: simulated diffraction image of the bulk hematite, containing a few indexed planes.

Figure 2b shows the SAED of Figure 2a in the top panel, where a typical single crystal pattern is observed. The simulation of this SAED pattern allowed the indexing of the crystalline planes (bottom panel of Figure 2b), indicating that this 2D material is oriented along the [001] zone axis. Moreover, as indicated by the blurred points in Figure 2b (top image), the SAED pattern presents extra points, indicating the misalignment of sheets along the $\langle hk0 \rangle$ direction.

We used an atomic force microscope (AFM) to probe the sample topography and thickness. Using an optical microscope, we could detect a ringlike pattern of the dried sample on the Si surface. The rings were composed of a dark substance with no apparent structural ordering, and by selecting an area between two of the rings, we detected small particles presenting a plateau-like morphology, which is shown in Figure 3. A seemingly crystalline core is identified from the red peaks, which are surrounded by a layer of amorphous material. The thickness of the amorphous material, which was identified as residual DMF, was 4 nm.

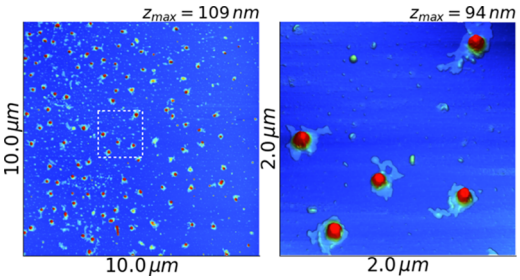

Figure 3. (Left) AFM image of a 10 μm × 10 μm area, (right) magnification of the 2 μm × 2 μm area depicted by the dashed square on the left image. The color code corresponds to the height of each pixel, where blue is the reference (zero) and red is the maximum height, shown on top of each panel.

Statistical analysis of the thickness distribution was performed using automated grain detection after polynomial background removal for each layer thickness interval as implemented in Gwyddion 2.50.[31] Such an analysis resulted in the detection of samples presenting thickness ranging from 5 to 110 nm, as shown in the histogram in Figure S6c (see the Supporting Information). Further analysis of the particles' morphology showed that, in the case of the very thin samples, it is impossible to distinguish hematite from DMF, which seems to be spread all over the substrate, contributing for the large thin species count. On the other hand, it is possible to notice in most particles, a plateau-like profile with smooth borders, suggesting the detection of a 2D material covered with DMF.

Theoretical Results. The formation energy per Fe_2O_3 unit (ΔE_f) vs number of layers (n) plot is presented in Figure 4a. A fit of eq 1 is also presented, and the formation energy of the bulk structure is depicted by the dashed horizontal line (ΔE_f^{bulk} = −8.85 eV per unit). The fitting parameters are E_0 = −8.83 eV, E_1 = 1.48 eV, and λ = −1.00. A decay of the form $1/n$ is obtained, as expected, and the formation energy for the bulk limit ($n \rightarrow \infty$) presents a deviation of 0.2% from the bulk formation energy, which is within the DFT energy error.

Using the fitted parameters into eq 2, the probability distribution with respect to the thickness t was calculated from a single layer (t = 0.4 nm) of hematite up to 1000 layers, and the result is plotted in Figure 4b. From that distribution, one can learn that the probability of observing very thin structures, e.g., $t \leq 10$ nm is very small [$p(t \leq 10\ \text{nm}) < 6.7 \times 10^{-4}$]. For comparison, eq 1 was fitted for n-layered graphene [$1 \leq n \leq 10$, see Figure S6a], and the same probability was calculated, resulting in $p(n \leq 10\ \text{nm}) < 1.9 \times 10^{-2}$.

DOI: 10.1021/acs.jpcc.9b01046
J. Phys. Chem. C 2019, 123, 16359−16365

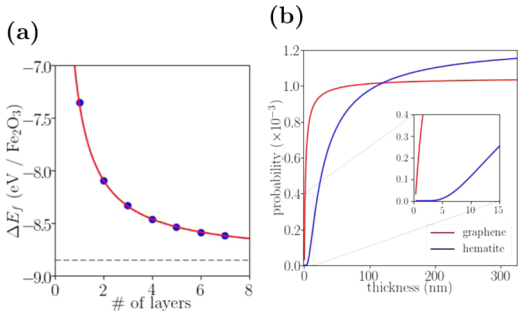

Figure 4. (a) Formation energy (ΔE_f) per Fe_2O_3 formula unit as a function of number of layers (n). Data points are blue filled circles, while the nonlinear fitting (eq 1) is the red line. Reference ΔE_f of the bulk α-Fe_2O_3 is depicted as a dashed horizontal line. (b) Probability distribution vs thickness for both hematite and graphene, calculated using the fitted parameters E_1 and λ in eq 2. Inset shows a nearly zero probability for small t in the case of hematite.

Using the AF_1 magnetic ground state ordering, we obtained the lattice parameter of the 1L phase (a = 5.175 Å, 2.8% larger than the experimental bulk value a = 5.035 Å[32]), as well as the phonon band structures and the corresponding density of the states for all structures, which are presented in Figure 5. No imaginary frequencies were obtained in either case, signaling the structural stability of the layered structures at T = 0 K.

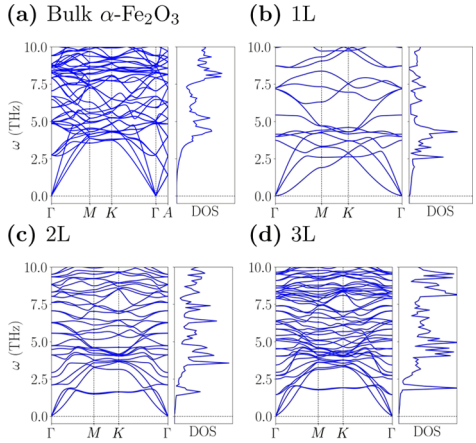

Figure 5. Phonon band structure and density of states. (a) Hexagonal bulk α-Fe_2O_3, (b) 1L, (c) 2L, and (d) 3L.

Orbital-projected band structure plots are presented for both spin-up and spin-down channels for the ground-state magnetic ordering AF_1 in Figure 6. It shows that in all structures, the conduction band minima (CBM) is mainly composed of Fe(d) contribution, while the valence band maxima (VBM) is of the O(p) nature. Real-space projections of both VBM and CBM are presented for the 1L in Figure 1b,c, respectively. Such projections show a d-like orbital located at the Fe atoms at the surfaces (CBM), while the VBM is composed mainly of the orbitals located at the O atoms and the Fe inner layer of the structure.

All layered structures showed a split between the spin channels, while for the bulk α-Fe_2O_3, both spin channels are degenerate. The band gap of the bulk is compatible with the experimental value (indirect E_g = 1.9 and direct E_g = 2.7 eV[33]), while the layered structures present smaller values of this quantity. In all cases, the band gap is indirect: for the bulk α-Fe_2O_3, the gap is between a point in the M−K direction and M, while for the layered structures, it is always a K−Γ excitation.

The magnetic ordering of hematite has been extensively debated in the literature.[34−36] The consensus is that in its bulk form, hematite is a weak ferromagnet between the Néel temperature (T_N = 961 K) and the Morin temperature (T_M = 260 K). In this temperature range, the localized iron spins are almost perpendicular to the c-axis of the hexagonal unit cell, with alternating orientations between the Fe layers. We define a layer in this case as the set of all Fe atoms located between the two closest [001] planes containing oxygen atoms, which are in turn depicted as red planes in Figure 7. Below T_M, the spins become collinear, with the aforementioned axis retaining an AFM arrangement between the layers (see Figure 8a).

According to our total energy calculations, the magnetic ground state for both the bulk α-Fe_2O_3 and the layered structures is AFM with the Fe localized moments coupled antiferromagnetically between the adjacent layers and ferromagnetically within a layer. This is in agreement with previous theoretical works, which reported the same magnetic orderings as well as similar energy differences.[23] For all structures, this magnetic ordering was labeled AF_1. The energy differences with respect the ground state are presented in Table 1.

The mapping of several DFT simulations of different magnetic orderings (σ) into the Heisenberg Hamiltonian (eq 3) enabled the calculation of the exchange couplings for all the structures studied in this work. The couplings and the corresponding Fe−Fe distances for all the structures are summarized in Table 2 and shown as colored double-headed arrows in Figure 7. For the bulk structure, we obtained the total energies for the ferromagnetic (E^{FM}) ordering and three different AFM orderings: (i) in the ground state, the spins on the neighboring Fe layers couple antiferromagnetically but couple ferromagnetically (E^{AF_1}) within the layer; (ii) in same layer, the spins couple antiferromagnetically (E^{AF_2}); and (iii) a combination of the previous two orderings consisting of four AFM couplings and two FM couplings between layers (E^{AF_3}). The three AFM configurations for bulk α-Fe_2O_3 are shown in Figure 8. Using these configurations and the corresponding energies, a set of equations was obtained for the calculation of J_{ij} for the hexagonal α-Fe_2O_3 (see the Supporting Information), and the resulting J_{ij} are presented in Table 2.

The same procedure was adopted for the 1−3L structures. In the case of 1L, the two Fe atoms located in the inner layer relaxed to a configuration where they were located at a common [001] plane. The magnetic orderings used to obtain the total energies via DFT calculations and the corresponding set of equations for the calculation of J_{ij} are shown in the Supporting Information.

All layered structures presented a nonvanishing total magnetic moment. Values of −0.211, −0.142, and −0.162 μ_B were obtained for 1L, 2L, and 3L, respectively, while no net magnetic moment was present in the bulk α-Fe_2O_3. The reason for that difference lies in the fact that for the layered structures, the Fe atoms in the uppermost and bottommost layers are in distinct chemical environment, i.e., present a distinct number of coordination with the surrounding O atoms, than the same atoms in the inner layers. In fact, the absolute value of the calculated moments for these outer Fe atoms are 3.98, 4.03, and 4.02 μ_B, while the bulk moments are in the range 4.14−4.17 μ_B.

DISCUSSION

A novel route for the synthesis of layered α-Fe_2O_3, based on synthetic hematite, is presented. Characterization via HRTEM

DOI: 10.1021/acs.jpcc.9b01046
J. Phys. Chem. C 2019, 123, 16359−16365

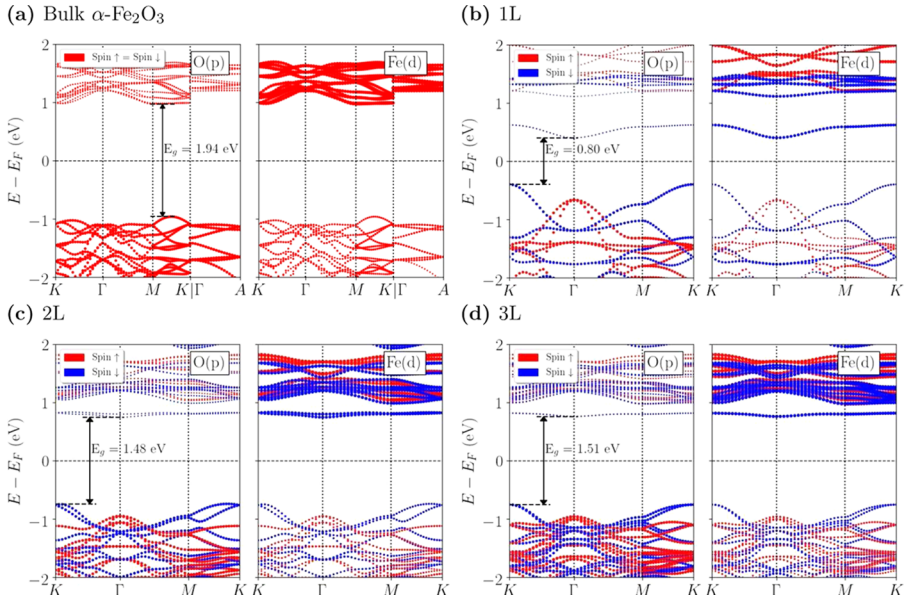

Figure 6. Electronic band structure projected on atomic orbitals. (a) Hexagonal bulk α-Fe_2O_3, (b) 1L, (c) 2L, and (d) 3L. The Fermi level is taken as a reference for all energies. The marker size corresponds to the orbital contribution to each band, and the color code depicts the two spin channels.

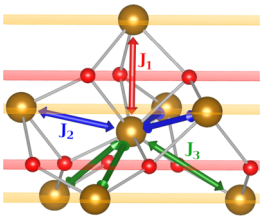

Figure 7. Cut from the hexagonal bulk α-Fe_2O_3, where the [001] planes containing the neighbors to a selected Fe atom are shown. The red vertical arrow corresponds to J_1, while blue and green arrows correspond to J_2 and J_3, respectively. Large golden spheres are Fe atoms, while small red spheres correspond to O atoms. Red and golden planes contain O and Fe atoms, respectively.

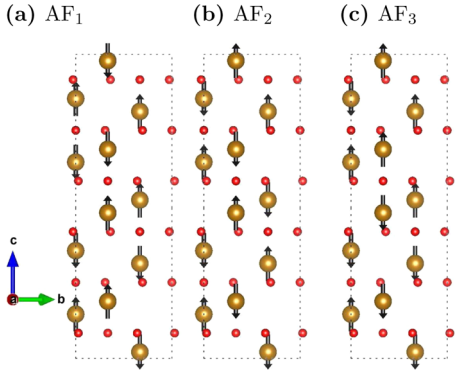

Figure 8. Three distinct AFM orderings for hexagonal α-Fe_2O_3: (a) AFM coupling between Fe layers, (b) AFM coupling within each layer, and (c) a combination of both orderings. The black arrows represent the localized spins in the Fe atoms (golden large spheres), while no significant moment is present in the O atoms (red smaller spheres).

Table 1. Energy Differences (in meV) Per Formula Unit between Magnetic Orderings with Respect to the AF_1 Ground State for the Bulk α-Fe_2O_3 as well as 1L, 2L, and 3L[a]

	$\Delta E_{AF_1-AF_2}$	$\Delta E_{AF_1-AF_3}$	ΔE_{AF_1-FM}
bulk	276	327	537
1L	214		562
2L	336	165	461
3L	232	265	518

[a]For 1L only the AF_1, AF_2, and FM orderings were considered due to the limited number of Fe atoms present in the structure.

Table 2. Classification of Exchange Couplings J_{ij} According to Fe−Fe Distances (d)[a]

	bulk			1L		
	J_1	J_2	J_3	J_1	J_2	J_3
distance (Å)	2.90	2.99	3.40	2.81	2.95	3.16
value (meV)	−25.9	8.7	−5.7		−3.6	−30.0
	2L			3L		
	J_1	J_2	J_3	J_1	J_2	J_3
distances (Å)	2.83	2.95	3.16	2.82	3.04	3.42
		2.98	3.50	2.89	2.98	3.40
					2.99	3.50
value (meV)	−8.5	−21.0	−23.2	−40.3	7.4	−4.9

[a]For the single layered structure, no value of J_1 is provided, since this particular coupling is not present in the structure (see Figures 7 and S1). The double- and triple-layered structures present more than one value for some distances because the structural relaxation leads to a break in the translational symmetry of the system along the c-axis, and the edge layers relax in a distinct way with respect to the bulk structure.

and SAED results in the detection of nanometer-sized, layered structures exposing the [001] surfaces predominantly. Thickness ranging from 5 nm up to 110 nm is obtained from AFM probing, signaling an abundance of multilayered structures. Nonetheless, the structural data obtained from the simulations point to the stability of all layered structures at T = 0 K. This means that in principle, the structures as thin as a single layer of hematite could be observed experimentally without the need of a supporting substrate to ensure its stability. However, the calculation of the formation energy per formula unit shows that the exfoliation of a single layer of hematite requires a much higher energy than a multilayered material. This statement is

DOI: 10.1021/acs.jpcc.9b01046
J. Phys. Chem. C 2019, 123, 16359−16365

supported both by the AFM data and the probability distribution calculated using eq 2. Thus, the probability of finding layered structures containing a number of layers ($t \geq 5$ nm) increases rapidly, in contrast to fewer layers, which are very unlikely to be detected. From the integration of the probability distribution up to $t = 10$ nm [$p(t \leq 10\ \text{nm}) \approx 6.7 \times 10^{-4}$], we conclude that, disregarding the solvation effects, the abundance of structures of that thickness is only 1 in 1500 approximately. The abundance of graphene is much higher, 1 in 53 (see Supporting Information). An explanation for such a large difference is simply the strength of the interlayer interaction, which for graphene is the much weaker van der Waals interaction in comparison to the covalent bonding in hematite. Nonetheless, it is possible, in principle, to obtain few-layer freestanding samples. A statistical sampling of the AFM data after the removal of DMF from the samples is pointed as a possible way of further exploring the thickness distribution of the layered material.

The energetic stability of the different magnetic orderings studied in this work is in fair agreement with the previous GGA +U theoretical works on the bulk and [001] surfaces of α-Fe_2O_3.[22,23] A similar interplanar distance contraction was found for the outermost layers of the thicker (2L and further) slabs, and a corresponding deviation from the bulk value for the magnetic moments of the Fe atoms was also detected (see Figure S7). The inner Fe layers present a magnetic moment nearly identical to the bulk value (deviation smaller than 0.05%), while deviations of 4.4 and 3.7% are observed for the surface atoms of 1L and thicker slabs, respectively. Moreover, the unpaired moments of the surface atoms give rise to a weak ferromagnetism in layered hematite, which is compatible to the previous theoretical works on the [001] surface,[22] but not in line with the calculations presented by Puthirath Balan et al., who report a ferromagnetic material.[13] Our finding is supported by the experimental data of the hysteresis curves as well as field-cooled and zero-field-cooled experiments.[13] Our interpretation is that the Fe atoms at the surfaces of the layered structures are responsible for the nonvanishing net magnetic moment that gives rise to ferromagnetism. For all layered structures, the AF_1 ordering, which can be described as alternating spin sublattices along the [001] planes, resulted in the lowest total energies for our spin-polarized calculations, in accordance with the theoretical results on the bulk and [001] surfaces.[22,23]

The mapping into the Heisenberg Hamiltonian provided values for the exchange coupling J_{ij} that support this statement in case the case of 3L. J_1 and J_3, which couple distinct spin sublattices (Fe planes along the [001] direction), are negative, i.e., they favor AFM coupling, while J_2, which couples spins within the same sublattice, is positive, describing a FM coupling for the bulk and 3L structures. In fact, the exchange couplings obtained for these two structures are quite similar, in contrast to the other 1L and 2L layered systems. This can be explained by the structural similarity between the bulk and 3L, which present similar Fe−Fe distances for the majority of the layers of the structure. On the other hand, for 1L and 2L, most of the distances are shorter than that in the bulk, since the ratio of the number of surface layers to bulk layers is larger in this case. For thicker layered structures, one expects that similarities with the bulk become even more pronounced.

The electronic band structures of 1L, 2L, and 3L show that the layered α-Fe_2O_3 presents a narrower band gap than the bulk. It evidences that no quantum confining effects are present, in principle, in the layered materials. The character of the CBM as well as the VBM are mostly preserved with respect to the bulk, Fe(d) and O(p), respectively, which means that both layered and bulk structures are described as charge-transfer insulators. The narrowing of the band gap with respect to bulk in this case can be explained by a reduced coordination of the surface Fe atoms, and the corresponding change of local symmetry, which leads to narrowing and shifting of the states derived from the Fe(d) orbitals, in accordance to previous theoretical studies.[22] The 1L band structure presents a defectlike electronic band at approximately 0.5 eV above the Fermi energy. Its small dispersion suggests that this level could, in principle, act as an electron trap, specially in the $M-K$ direction, where it becomes more localized. This very same band shifts to energies closer to the CBM and becomes a doublet for the 2L and 3L structures, and their dispersion is even smaller. In all cases, its major contribution is of the d orbitals located at the Fe atoms at the exposed surfaces. Extrapolation of these results for thicker samples suggest that that charge trapping could be feasible in the surfaces of layered structures, and their application as a photocatalyst materials is possible.

CONCLUSIONS

Electron and atomic force microscopy images show layered structures of hematite obtained via a novel synthetic route. Thickness of the samples is estimated to range from 5 nm up to 110 nm, while the first-principles calculations describe single-, double-, and triple-layered structures of hematite as stable at $T = 0$ K. The thickness distribution of the 2D hematite is obtained using the first-principles calculations and Boltzmann statistics, which tells us that the probability of obtaining structures thinner than 10 nm is very small [$p(t \leq 10\ \text{nm}) < 6.7 \times 10^{-4}$], i.e., we expect to find one sample with 0.4 nm $\leq t \leq$ 10 nm for each 1500 samples.

Our results point to a weak ferromagnetic material, where adjacent spin lattices located parallel to the [001] planes couple antiferromagnetically, while the Fe atoms at the exposed surfaces, which present a deviation of their magnetic moments with respect to the bulk value, contribute to a nonvanishing total magnetic moment. The calculation of the exchange couplings J_{ij} from the Heisenberg model support this finding. The electronic bands show a narrower band gap of the layered structures in comparison to the bulk owing to the distinct coordination, and thus distinct local symmetry of the Fe atoms at the surface, which impacts the Fe(d) levels that contribute to the conduction band in this material. The possible acceptor charge-trapping levels located at the Fe atoms at the exposed surface are also highlighted.

ASSOCIATED CONTENT

Supporting Information

The Supporting Information is available free of charge on the ACS Publications website at DOI: 10.1021/acs.jpcc.9b01046.

Magnetic orderings and associated set of equations for the calculation of the J_{ij} parameters of the Heisenberg Hamiltonian, sample preparation SEM images, HRTEM images, formation energies, and probability of occurrence of samples with respect to the number of layers, as well as analysis of interplanar distance contraction and expansion of the layered materials and comparison to the bulk values (PDF)

DOI: 10.1021/acs.jpcc.9b01046
J. Phys. Chem. C 2019, 123, 16359−16365

AUTHOR INFORMATION

Corresponding Author

*E-mail: claudio.padilha@lnnano.cnpem.br.

ORCID

A. C. M. Padilha: 0000-0003-1697-2800

Notes

The authors declare no competing financial interest.

ACKNOWLEDGMENTS

The authors acknowledge the support of São Paulo Research Foundation (Fapesp) in form of the grants 2018/05565-0 and 2017/02317-2. Computational resources from the National Laboratory of Scientific Computing (LNCC) were used for all calculations presented in this work. The HRTEM images were obtained by J. Bettini, and the AFM images were obtained by C. Costa and C. Biffe by means of the microscopy facilities at LNNano/CNPEM. A.C.M.P. would like to express gratitude for the helpful discussions with M. T. Costa and G. R. Schleder.

REFERENCES

(1) Novoselov, K. S.; Geim, A. K.; Morozov, S. V.; Jiang, D. A.; Zhang, Y.; Dubonos, S. V.; Grigorieva, I. V.; Firsov, A. A. Electric Field Effect in Atomically Thin Carbon Films. *Science* **2004**, *306*, 666−669.

(2) Tan, C.; Cao, X.; Wu, X. J.; He, Q.; Yang, J.; Zhang, X.; Chen, J.; Zhao, W.; Han, S.; Nam, G. H.; et al. Recent Advances in Ultrathin Two-Dimensional Nanomaterials. *Chem. Rev.* **2017**, *117*, 6225−6331.

(3) Paul, J.; Singh, A.; Dong, Z.; Zhuang, H.; Revard, B.; Rijal, B.; Ashton, M.; Linscheid, A.; Blonsky, M.; Gluhovic, D.; et al. Computational Methods for 2D Materials: Discovery, Property Characterization, and Application Design. *J. Phys.: Condens. Matter* **2017**, *29*, No. 473001.

(4) Singh, A. K.; Mathew, K.; Zhuang, H. L.; Hennig, R. G. Computational Screening of 2D Materials for Photocatalysis. *J. Phys. Chem. Lett.* **2015**, *6*, 1087−1098.

(5) Liu, Q.; Zhang, X.; Abdalla, L. B.; Fazzio, A.; Zunger, A. Switching a Normal Insulator into a Topological Insulator via Electric Field with Application to Phosphorene. *Nano Lett.* **2015**, *15*, 1222−1228.

(6) Padilha, J. E.; Fazzio, A.; Da Silva, A. J. Van der Waals Heterostructure of Phosphorene and Graphene: Tuning the Schottky Barrier and Doping by Electrostatic Gating. *Phys. Rev. Lett.* **2015**, *114*, No. 066803.

(7) Padilha, J. E.; Lima, M. P.; Da Silva, A. J.; Fazzio, A. Bilayer Graphene Dual-Gate Nanodevice: An ab initio Simulation. *Phys. Rev. B* **2011**, *84*, No. 113412.

(8) Pontes, R. B.; Miwa, R. H.; da Silva, A. J.; Fazzio, A.; Padilha, J. E. Layer-Dependent Band Alignment of Few Layers of Blue Phosphorus and Their van der Waals Heterostructures with Graphene. *Phys. Rev. B* **2018**, *97*, No. 235419.

(9) Alvarez-Quiceno, J. C.; Miwa, R. H.; Dalpian, G. M.; Fazzio, A. Oxidation of Free-Standing and Supported Borophene. *2D Mater.* **2017**, *4*, No. 025025.

(10) Alvarez-Quiceno, J. C.; Schleder, G. R.; Marinho, E.; Fazzio, A. Adsorption of 3d, 4d, and 5d Transition Metal Atoms on β 12-Borophene. *J. Phys.: Condens. Matter* **2017**, *29*, No. 305302.

(11) Duong, D. L.; Yun, S. J.; Lee, Y. H. Van der Waals Layered Materials: Opportunities and Challenges. *ACS Nano* **2017**, *11*, 11803−11830.

(12) Mounet, N.; Gibertini, M.; Schwaller, P.; Campi, D.; Merkys, A.; Marrazzo, A.; Sohier, T.; Castelli, I. E.; Cepellotti, A.; Pizzi, G.; et al. Two-Dimensional Materials from High-Throughput Computational Exfoliation of Experimentally Known Compounds. *Nat. Nanotechnol.* **2018**, *13*, 246−252.

(13) Puthirath Balan, A.; Radhakrishnan, S.; Woellner, C. F.; Sinha, S. K.; Deng, L.; Reyes, C. D. L.; Rao, B. M.; Paulose, M.; Neupane, R.; Apte, A.; et al. Exfoliation of a Non-van der Waals Material From Iron Ore Hematite. *Nat. Nanotechnol.* **2018**, *13*, 602−609.

(14) Puthirath Balan, A.; Radhakrishnan, S.; Kumar, R.; Neupane, R.; Sinha, S. K.; Deng, L.; De Los Reyes, C. A.; Apte, A.; Rao, B. M.; Paulose, M. A Non-van der Waals 2D Material from Natural Titanium Mineral Ore Ilmenite. *Chem. Mater.* **2018**, *30*, 5923−5931.

(15) Yadav, T. P.; Shirodkar, S. N.; Lertcumfu, N.; Radhakrishnan, S.; Sayed, F. N.; Malviya, K. D.; Costin, G.; Vajtai, R.; Yakobson, B. I.; Tiwary, C. S.; et al. Chromiteen: A New 2D Oxide Magnetic Material from Natural Ore. *Adv. Mater. Interfaces* **2018**, *5*, No. 1800549.

(16) Gou, X.; Wang, G.; Park, J.; Liu, H.; Yang, J. Monodisperse Hematite Porous Nanospheres: Synthesis, Characterization, and Applications for Gas Sensors. *Nanotechnology* **2008**, *19*, No. 125606.

(17) Kresse, G.; Hafner, J. Ab Initio Molecular Dynamics for Liquid Metals. *Phys. Rev. B* **1993**, *47*, 558−561.

(18) Kresse, G.; Hafner, J. Ab Initio Molecular-Dynamics Simulation of the Liquid-Metal-Amorphous-Semiconductor Transition in Germanium. *Phys. Rev. B* **1994**, *49*, 14251−14269.

(19) Perdew, J. P.; Burke, K.; Ernzerhof, M. Generalized Gradient Approximation Made Simple. *Phys. Rev. Lett.* **1996**, *77*, 3865−3868.

(20) Blöchl, P. E. Projector Augmented-Wave Method. *Phys. Rev. B* **1994**, *50*, 17953−17979.

(21) Dudarev, S.; Botton, G.; et al. Electron-Energy-Loss Spectra and the Structural Stability of Nickel Oxide: An LSDA+U Study. *Phys. Rev. B* **1998**, *57*, 1505−1509.

(22) Rohrbach, A.; Hafner, J.; Kresse, G. Ab Initio Study of the (0001) Surfaces of Hematite and Chromia: Influence of Strong Electronic Correlations. *Phys. Rev. B* **2004**, *70*, No. 125426.

(23) Rollmann, G.; Rohrbach, A.; Entel, P.; Hafner, J. First-Principles Calculation of the Structure and Magnetic Phases of Hematite. *Phys. Rev. B* **2004**, *69*, No. 165107.

(24) Negreiros, F. R.; Pedroza, L. S.; Dalpian, G. M. Effect of Charges on the Interaction of a Water Molecule with the Fe_2O_3(0001) Surface. *J. Phys. Chem. C* **2016**, *120*, 11918−11925.

(25) Momma, K.; Izumi, F. VESTA 3 for Three-Dimensional Visualization of Crystal, Volumetric and Morphology Data. *J. Appl. Crystallogr.* **2011**, *44*, 1272−1276.

(26) Blake, R. L.; Hessevic, R. E.; Zoltai, T.; Finger, L. W. Refinement of the Hematite Structure. *Am. Mineral.* **1966**, *51*, 123−129.

(27) Togo, A.; Tanaka, I. First Principles Phonon Calculations in Materials Science. *Scr. Mater.* **2015**, *108*, 1−5.

(28) Vinet, P.; Smith, J. R.; Ferrante, J.; Rose, J. H. Temperature Effects on the Universal Equation of State of Solids. *Phys. Rev. B* **1987**, *35*, 1945−1953.

(29) Ashcroft, N. W.; Mermin, N. D. *Solid State Physics*; Saunders College: Philadelphia, 1976.

(30) Da Silva, A. J. R.; Fazzio, A.; Dos Santos, R. R.; Oliveira, L. E. Disorder and the Effective Mn-Mn Exchange Interaction in $Ga_{1-x}Mn_x$ As Diluted Magnetic Semiconductors. *Phys. Rev. B* **2005**, *72*, No. 125208.

(31) Nečas, D.; Klapetek, P. Gwyddion: An open-source software for SPM data analysis. *Open Phys.* **2012**, *10*, 181−188.

(32) Maslen, E. N.; Streltsov, V. A.; Streltsova, N. R.; Ishizawa, N. Synchrotron X-Ray Electron Density in the Layered LaOCl Structure. *Acta Crystallogr., Sect. B: Struct. Sci.* **1996**, *52*, 576−579.

(33) Glasscock, J. A.; Barnes, P. R. F.; Plumb, I. C.; Bendavid, A.; Martin, P. J. Structural, Optical and Electrical Properties of Undoped Polycrystalline Hematite Thin Films Produced Using Filtered Arc Deposition. *Thin Solid Films* **2008**, *516*, 1716−1724.

(34) Hill, A. H.; Jiao, F.; Bruce, P. G.; Harrison, A.; Kockelmann, W.; Ritter, C. Neutron Diffraction Study of Mesoporous and Bulk Hematite, α-Fe_2O_3. *Chem. Mater.* **2008**, *20*, 4891−4899.

(35) Grønvold, F.; Sawelsen, E. J. Heat Capacity and Thermodynamic Properties of α-Fe_2O_3 in the Region 300−1050 K. Antiferromagnetic Transition. *J. Phys. Chem. Solids* **1975**, *36*, 249−256.

(36) Morin, F. J. Magnetic Susceptibility of αFe_2O_3 and αFe_2O_3 with Added Titanium. *Phys. Rev.* **1950**, *78*, 819−820.

DOI: 10.1021/acs.jpcc.9b01046
J. Phys. Chem. C 2019, 123, 16359−16365